New modeling approach of secondary control layer for autonomous single-phase microgrids

BENDIB, Ahmed, CHOUDER, Aissa, KARA, Kamel, KHERBACHI, Abdelhammid, BARKAT, Said and ISSA, Walid <http://orcid.org/0000-0001-9450-5197>

Published version

BENDIB, Ahmed, CHOUDER, Aissa, KARA, Kamel, KHERBACHI, Abdelhammid, BARKAT, Said and ISSA, Walid (2019). New modeling approach of secondary control layer for autonomous single-phase microgrids. Journal of the Franklin Institute, 356 (13), 6842-6874.

Accepted Manuscript

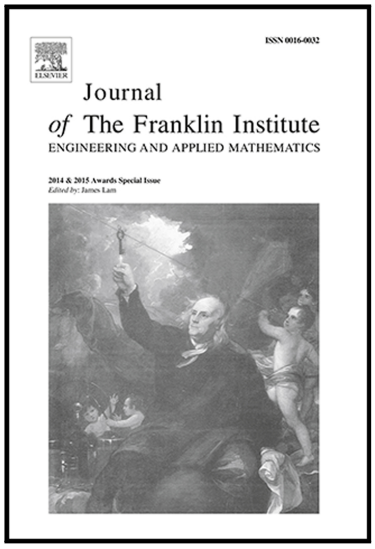

New Modeling Approach of Secondary Control Layer for Autonomous Single-Phase Microgrids

Ahmed Bendib, Aissa Chouder, Kamel Kara,
Abdelhammid Kherbachi, Said Barkat, Walid Issa

PII: S0016-0032(19)30268-6
DOI: https://doi.org/10.1016/j.jfranklin.2019.04.020
Reference: FI 3895

To appear in: *Journal of the Franklin Institute*

Received date: 3 October 2018
Revised date: 14 February 2019
Accepted date: 8 April 2019

Please cite this article as: Ahmed Bendib, Aissa Chouder, Kamel Kara, Abdelhammid Kherbachi, Said Barkat, Walid Issa, New Modeling Approach of Secondary Control Layer for Autonomous Single-Phase Microgrids, *Journal of the Franklin Institute* (2019), doi: https://doi.org/10.1016/j.jfranklin.2019.04.020

Highlights

- New modeling approach of the secondary control for single-phase microgrid is proposed.
- SOGI-FLL dynamics are introduced in the modeling of the secondary control layer.
- Amplitude dynamic model of SOGI-FLL is derived based on phasor theory.
- Tuning procedure for the proper selection of the control parameters is discussed.
- The proposed control approach is tested under various disturbances.
- The results validate the proposed approach to achieve the desired transient response.

New Modeling Approach of Secondary Control Layer for Autonomous Single-Phase Microgrids

Ahmed Bendib[a,*], Aissa Chouder[b], Kamel Kara[a], Abdelhammid Kherbachi[a], Said Barkat[b], Walid Issa[c]

[a] *SET Laboratory, Electronics Department, Blida 1 University, BP 270 Blida, Algeria*
[b] *Electrical Engineering Laboratory, University Mohamed Boudiaf, Msila, BP 166, 28000, Algeria*
[c] *Electrical and Electronic Engineering Department, Sheffield Hallam University, S1 1WB, UK*

Abstract

In a microgrid (MG) topology, the secondary control is introduced to compensate for the voltage amplitude and frequency deviations, mainly caused by the inherent characteristics of the droop control strategy. This paper proposes an accurate approach to derive small signal models of the frequency and amplitude voltage at the point of common coupling (PCC) of a single-phase MG by analyzing the dynamics of the second-order generalized integrator-based frequency-locked loop (SOGI-FLL). The frequency estimate model is then introduced in the frequency restoration control loop, while the derived model of the amplitude estimate is introduced for the voltage restoration loop. Based on the obtained models, the MG stability analysis and proposed controllers' parameters tuning are carried out. Also, this study includes the modeling and design of the synchronization control loop that enables a seamless transition from island mode to grid-connected mode operation. Simulation and practical experiments of a hierarchical control scheme, including traditional droop control and the proposed secondary control for two single-phase parallel inverters, are implemented to confirm the effectiveness and the robustness of the proposal under different operating conditions. The obtained results validate the proposed modeling approach to provide the expected transient response and disturbance rejection in the MG.

Keywords: `Single-phase microgrid, Secondary control, Frequency and voltage restoration, Modeling, SOGI-FFL dynamics, Synchronization`

1. Introduction

Microgrids (MGs) are local electrical networks, which are designed for efficient, reliable and flexible use of distributed generators (DGs) including renewable energy sources and energy storage devices [1, 2, 3]. In such networks, the distributed generators are linked at the point of common coupling (PCC) via power converters enabling MGs to operate either in grid-connected mode or islanded mode [4, 5]. The control of power converters-based MG must be able to guarantee some objectives such as power-sharing, power quality enhancement, synchronization, and power flow management [6]. Toward this end, hierarchical control consisting of primary, secondary and tertiary controls is the most adopted scheme in the literature [7, 8, 9]]. The primary control is locally implemented to ensure power-sharing among DG units and their stable operation. Whereas, the secondary control is required to compensate for frequency and amplitude deviations caused by the inherent characteristics of the primary control, as well as ensuring power quality enhancement. In addition, when the grid connection mode is expected, microgrid synchronization to the main utility grid is included within the secondary control scope [10]. The tertiary controller deals with the power flow by providing the set points to the lower control levels.

*Corresponding author
Email addresses: `ahmeddib28@gmail.com` (Ahmed Bendib), `aissachouder@gmail.com` (Aissa Chouder), `km_kara@yahoo.fr` (Kamel Kara), `kherbachi.h@gmail.com` (Abdelhammid Kherbachi), `sa_barkati@yahoo.fr` (Said Barkat), `walid.issa@shu.ac.uk` (Walid Issa)

The secondary control, intended for frequency and amplitude restoration, has been considered for both single and three phase AC microgrids [11, 12, 13, 14, 15]. Two main strategies of the secondary control layer have been reported in the literature; centralized and distributed approaches [16, 17, 18, 19, 20, 21]. In the centralized control approach, a central controller is responsible for producing the DGs' control signals, based on the estimated microgrid parameters, i.e., frequency and amplitude. In this strategy, an underlying communication network is required to communicate the appropriate control signals to the primary control of each DG unit. While the distributed secondary control is locally implemented in each DG with the aim to improve the system reliability. This control strategy requires both local estimates and the measured parameters of interest of the rest of DG units, which are exchanged through a sparse communication network, to produce the required set points to the primary control. The above-mentioned approaches generally use the phase-locked loop (PLL) technique to estimate the frequency and amplitude of the microgrid at the PCC and those of other DG units. According to this estimation approach, the dynamic models of the secondary control for frequency and amplitude restoration have been derived by exploiting the small signal model of the PLL. For instance, [22] have modeled the centralized secondary control of a three-phase MG considering the PLL transfer function to express the frequency estimate dynamics in the frequency restoration. While the amplitude estimation is modeled as a unity gain for the amplitude restoration. Similarly, in [23], the PLL model has been used in the frequency recovery model for two different control strategies: model predictive controller and Smith predictor-based PI controller. However, the voltage recovery modeling has not been reported. The same concept has been adopted to model the distributed secondary control for frequency and amplitude restoration in [19], [24] and [25]. In [26], a unity voltage feedback has been considered in state space modeling of a distributed voltage control. It is worth mentioning here that all the available modeling approaches are proposed for three-phase MGs, in which only the frequency estimate dynamics has been taken into account, and the amplitude estimate has been modeled as a unity gain. This concept is valid for three-phase MGs, as the frequency is estimated by the PLL while the amplitude can be computed directly by using the $\alpha\beta$ voltage components that are obtained based on the $abc/\alpha\beta$ coordinate transformation. However, in single-phase MGs, both amplitude and frequency are estimated using the PLL, from a single-phase input voltage. Hence, the estimation dynamics of both of these variables should be taken into consideration in the frequency and amplitude restoration modeling. According to this reason, the authors in [27] have proposed a schematic diagram of the secondary control model for amplitude restoration of a single-phase MG. In fact, a first-order transfer function is introduced to describe the amplitude estimate dynamics. One should note that this is the only paper found in the existing literature which deals with this issue. However, the authors did not mention how this transfer function has been obtained and how its parameter has been selected. This is may be due to the difficulty of expressing the amplitude estimation dynamics from the PLL's small signal model. Hence, the analyses of the amplitude restoration control based on this model are not accurate. Consequently, an improper tuning of the control parameters and, then, the stability of the MG can be seriously compromised.

Although the existing literature has addressed extensively the frequency and amplitude restoration in the secondary layer for three-phase MGs and has covered all the modeling and control design aspects, there is still blind spots and challenging tasks regarding single-phase MGs. The main challenges related to the secondary control modeling in single-phase MGs, are listed below:

- Lack of precise modeling of microgrid frequency and voltage restoration control, more particularly, due to the unknown dynamics of the involved estimates
- Lack of a comprehensive tuning procedure for parameters selection of the proportional-integral (PI) controllers involved in the restoration control.

The present paper aims to derive accurate dynamic models of the secondary control layer for both frequency and amplitude restoration, intended for an islanded single-phase AC microgrid. To this end, the authors explore the main features of SOGI-FLL to get the transfer functions that describe the frequency and amplitude estimates dynamics and to introduce them into the overall secondary control modeling (see Fig. 1). Actually, the main contributions, in this paper, are listed hereafter:

- Dynamic phasor concept-based SOGI-FLL modeling is proposed to derive the amplitude estimate dynamic model. The derived model is, then, introduced as feedback in the amplitude restoration control

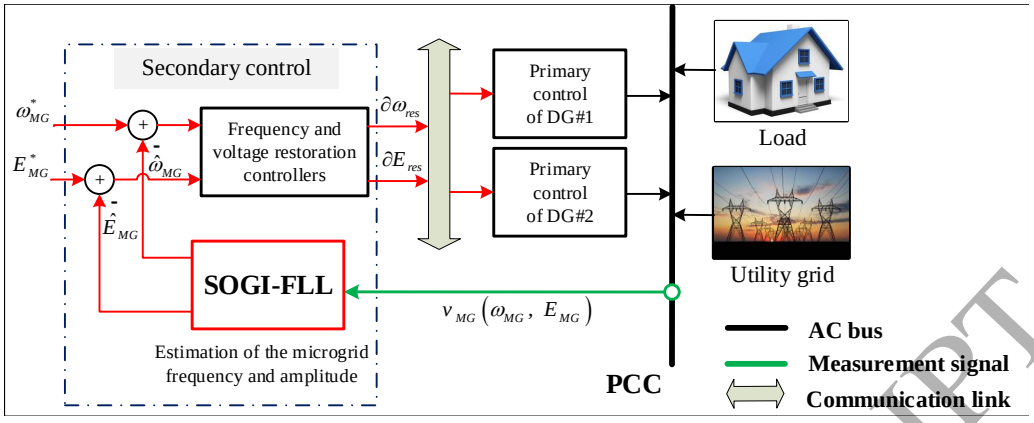

Figure 1: Hierarchical control of a single-phase AC microgrid considering primary control and secondary control based on SOGI-FLL for parameters estimation. The MG consists of two parallel DG units, in which each DG has its own local controller, connected to a local load and the utility grid at a common AC bus.

loop

- The linearized model of the frequency locked loop (FLL) is suggested as a frequency estimate model. This model is considered as a feedback in the frequency restoration control loop
- The stability analysis of the system and a systematic design process for a proper selection of the restoration controllers' parameter are performed
- The synchronization modeling and control design that enables a seamless transition from islanded mode to grid-connected mode operation are studied.

Simulation and experimental implementation of a hierarchical control scheme, including traditional droop control and the designed secondary control for two single-phase parallel-connected inverters, are carried out to assess the effectiveness of the proposal under various disturbances.

The rest of this paper is structured as follows. Section 2 describes the primary and proposed secondary controls of an autonomous single-phase AC microgrid. In Section 3, the proposed modeling approach of secondary control for frequency and voltage restoration is provided. In this section, the phasor theory-based SOGI-FLL modeling analysis is developed. Frequency and amplitude restoration modeling and tuning procedure, as well as the synchronization modeling and control design, are also presented in this section. Section 4 shows the simulation results of the microgrid including the proposed restoration and synchronization controls. Section 5 presents the experimental results of a designed platform based on ARM Cortex microcontrollers for the proposed control implementation. Finally, some conclusions are reported in section 6.

2. Proposed control scheme for single-phase AC microgrid

In Fig. 2, it shows the hierarchical control scheme for two parallel-connected single-phase inverters, forming an islanded AC MG. As depicted in Fig. 2, the power inverters-based DGs share the same AC bus through a line inductive impedance. The local load and the utility grid are also connected to this AC bus. Each DG unit consists of a voltage source inverter (VSI) fed by a DC source and associated to an LC filter allowing high-frequency content cancelation [28]. In this structure, the hierarchical control of the islanded MG is divided into two control levels: primary and secondary.

1) Primary control:
The primary control adopted in this work is based on the droop control method, which is the most employed strategy for islanded AC microgrids [29, 30]. This level is strictly local and is responsible for active and reactive power-sharing between DG units without any communication. According to Fig. 2, the

primary control layer includes, SOGI-FLL-based power calculations, droop controller, virtual impedance loop, and voltage and current control loops. The SOGI-FLL scheme is introduced to extract the orthogonal components of the output voltage and current, $v_{\alpha\beta}$ and $i_{\alpha\beta}$, of each DG unit, in order to calculate the average active and reactive powers (P and Q) by using the following expressions [31]:

$$\begin{cases} P_i = {}^1\!/_2 \left(\hat{v}_{i\alpha} \times \hat{i}_{i\alpha} + \hat{v}_{i\beta} \times \hat{i}_{i\beta} \right) \\ Q_i = {}^1\!/_2 \left(\hat{v}_{i\beta} \times \hat{i}_{i\alpha} - \hat{v}_{i\alpha} \times \hat{i}_{i\beta} \right) \end{cases} \tag{1}$$

where: $i = 1, 2$.

These calculated powers are used by the droop controller to generate the corresponding voltage frequency and amplitude, ω_i and E_i, according to the droop control functions, given by the following expressions:

$$\begin{cases} \omega_i = \omega^* - mP_i + \partial\omega_{res} \\ E_i = E^* - nQ_i + \partial E_{res} \end{cases} \tag{2}$$

where ω^* and E^* are the frequency and amplitude references respectively, m and n are the droop control coefficients. $\partial\omega_{res}$ and ∂E_{res} are the control signals received from the secondary control level in order to compensate for frequency and amplitude deviations.

In order to produce the voltage reference, v_i^*, across the capacitor of the output filter, the generated sinusoidal voltage using the droop control outputs is compared to the virtual impedance voltage (v_z), as expressed by the following equation:

$$v_i^*(t) = E_i \times \sin\left(\int \omega_i dt \right) - v_{zi}(t) \tag{3}$$

The produced reference voltage (v_i^*) is handled by an inner multi-loop control to provide the appropriate PWM pattern for each VSI. More details about the primary control can be found in [32].

2) Secondary control:

As the frequency and voltage at the PCC deviate from their nominal values due to the droop control characteristics, the secondary controller will bring them back to their rated values. The block diagram of the proposed secondary control, implemented in the MG central controller, is shown in Fig. 2. In this control level, SOGI-FLL estimates the microgrid's frequency and amplitude, as well as the orthogonal components of both microgrid and the utility grid. Then, two control loops; synchronization and restoration are built up. In the synchronization stage, the extracted orthogonal components are used to compute the phase angle difference between the MG and the utility grid and passes through a proportional (P) controller to be matched. The corresponding control signal is used to update the frequency reference in the restoration control loop. In the restoration stage, the estimated frequency and amplitude ($\hat{\omega}_{MG}$, $\hat{E}_{MG}$) are compared to the desired nominal values (ω_{MG}^*, E_{MG}^*) and processed through IP controllers to produce the required adjustments for the actual frequency and amplitude. The produced control signals i.e., $\partial\omega_{res}$ and ∂E_{res}, are sent to the primary control level, via a low bandwidth communication link, to recover the desired nominal values.

The expressions of the frequency and amplitude restoration compensators based on the IP-type controller can be expressed as follow:

$$\partial\omega_{res} = \int k_{i-f} \left((\omega_{MG}^* - \partial\omega_{syn}) - \omega_{MG} \right) dt - k_{p-f} \times \omega_{MG} \tag{4}$$

$$\partial E_{res} = \int k_{i-E} \left(E_{MG}^* - E_{MG} \right) dt - k_{p-E} \times E_{MG} \tag{5}$$

where k_{p-f}, k_{i-f}, and k_{p-E}, k_{i-E} are frequency and voltage controllers' gains, respectively, $\partial\omega_{syn}$ is the synchronization control signal, which is set to zero when the grid is not present.

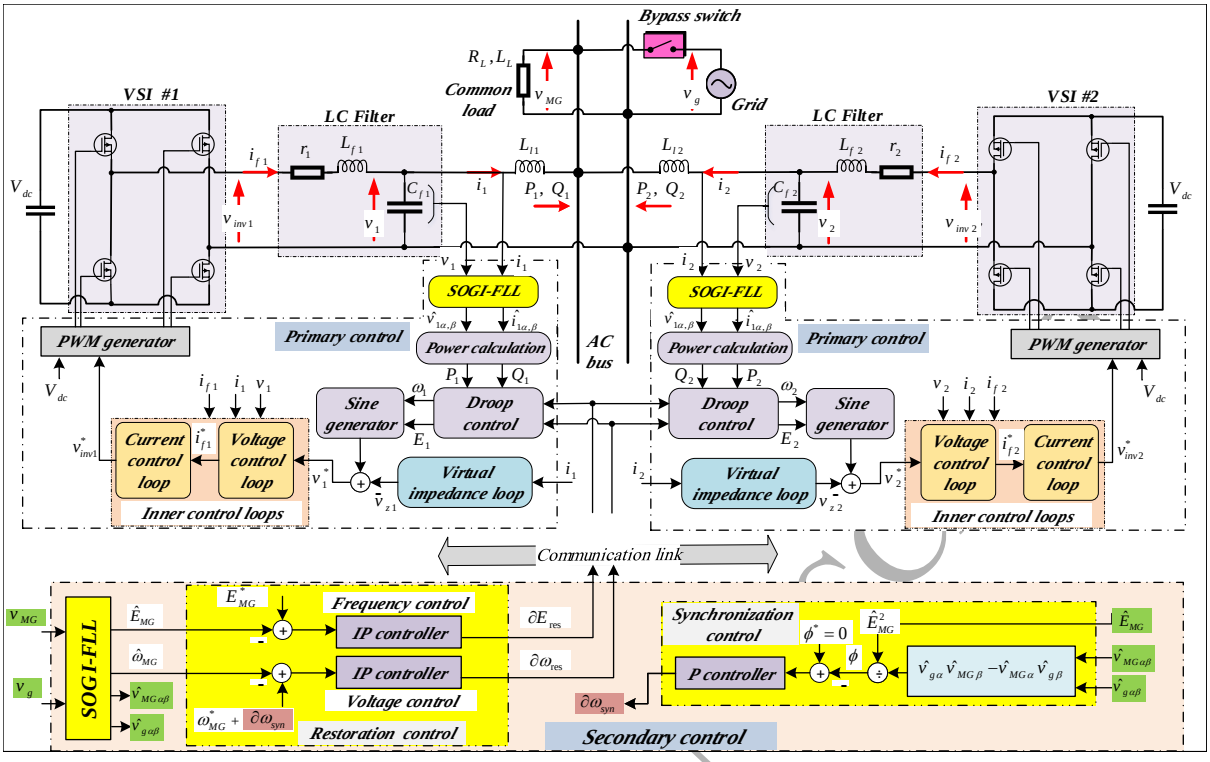

Figure 2: Hierarchical control scheme for two single-phase inverters-based islanded AC microgrid.

In order to analyze the microgrid stability and to select properly the parameters of the frequency and voltage secondary control, accurate dynamic models are developed. The proposed modeling approach to derive these models and the tuning procedure of the control parameters are presented in the next section.

3. Proposed modeling approach of the secondary control

The proposed modeling approach aims to obtain accurate dynamic models of the secondary control for frequency and amplitude restoration of a single-phase AC microgrid. The main idea of the proposed approach is that the frequency and amplitude estimates dynamics of SOGI-FLL, which should be derived, are exploited in the secondary control modeling. As depicted in Fig. 3, the restoration control model includes the models of; frequency/amplitude restoration control, communication delay, and SOGI-FLL frequency and amplitude estimates of the secondary control stage. In addition, the models of droop control, power calculations and the inner control loops of the primary control stage are introduced in the restoration model. Furthermore, the restoration model involved the line impedance model that describes the frequency and amplitude changes from DG units to the PCC.

The modeling of SOGI-FLL scheme is given in subsection below, where the frequency dynamics is concluded, while a theoretical analysis in the phasor domain is developed to obtain the voltage estimate dynamics. In the second subsection, the modeling of the frequency and amplitude restoration control based on the SOGI-FLL dynamics is developed, in which the dynamics of the inner controller is assumed to be negligible due to its fast response. Also, the line impedance model is considered negligible in the restoration modeling process. A tuning procedure based on the obtained mathematical models, as well as the synchronization modeling and design analysis are also investigated in other subsections.

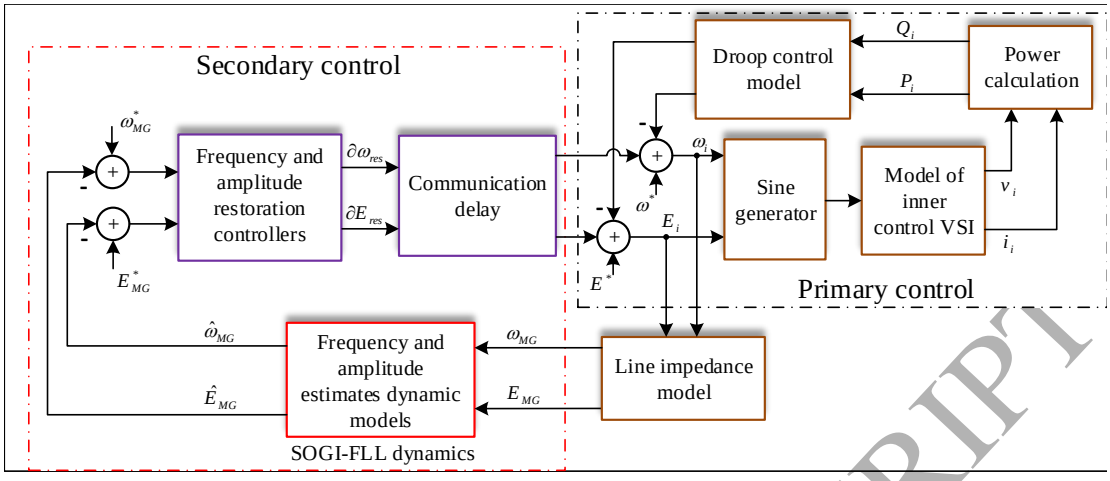

Figure 3: Model of the restoration control loop based on SOGI-FLL dynamics.

3.1. Modeling of SOGI-FLL

The SOGI-FLL scheme is an adaptive second-order filter used to estimate the key parameters of a single-phase input voltage [33]. The block diagram of SOGI-FLL structure is highlighted in Fig. 4. It consists of two main blocks; SOGI-based quadrature signal generator (SOGI-QSG) and FLL. The SOGI-QSG block is responsible for extracting the direct and the orthogonal voltage components that are used to calculate the voltage amplitude. While the FLL unit estimates the operating frequency to be fed to the SOGI-QSG block.

According to Fig. 4, the closed loop transfer functions which describe the relationship between the extracted orthogonal components ($\hat{v}_{MG\alpha}$, $\hat{v}_{MG\beta}$) and the input microgrid voltage can be given by:

$$G_{\alpha}(s) = \frac{\hat{v}_{MG\alpha}(s)}{v_{MG}(s)} = k\hat{\omega}_{MG}\frac{s}{s^2 + k\hat{\omega}_{MG}s + \hat{\omega}_{MG}^2} \tag{6}$$

$$G_{\beta}(s) = \frac{\hat{v}_{MG\beta}(s)}{v_{MG}(s)} = k\hat{\omega}_{MG}^2\frac{1}{s^2 + k\hat{\omega}_{MG}s + \hat{\omega}_{MG}^2} \tag{7}$$

where s is the Laplace variable, $\hat{\omega}_{MG}$ is the estimated frequency, and k is the SOGI-QSG gain, which is generally recommended to take the value $\frac{1}{\sqrt{2}}$ [33].

In addition, the simplified transfer function of the FLL frequency adaptation loop can be expressed as follows [34]:

$$\hat{\omega}_{MG} = \frac{\Gamma}{s + \Gamma}\omega_{MG} \tag{8}$$

where ω_{MG} is the input frequency, and Γ is the FLL gain, which is related to the FLL controller gain γ; given in Fig. 4; by the following expression [34]:

$$\gamma = \frac{k\hat{\omega}_{MG}}{\hat{E}_{MG}^2}\Gamma \tag{9}$$

As it can be noted, Eq. (8) which describes the relationship between the input frequency and the estimated one, can be considered as a model for the frequency estimation dynamics. While, for the dynamics of amplitude estimate, theoretical analysis in the phasor domain is developed to derive its corresponding model. The developed analysis is given hereafter.

According to Eq. (6), the differential equation describes the direct component ($\hat{v}_{MG\alpha}$) dynamics as a function of the input voltage (v_{MG}), can be written as:

$$\ddot{\hat{v}}_{MG\alpha} + k\hat{\omega}_{MG}\dot{\hat{v}}_{MG\alpha} + \hat{\omega}_{MG}^2\hat{v}_{MG\alpha} = k\hat{\omega}_{MG}\dot{v}_{MG} \tag{10}$$

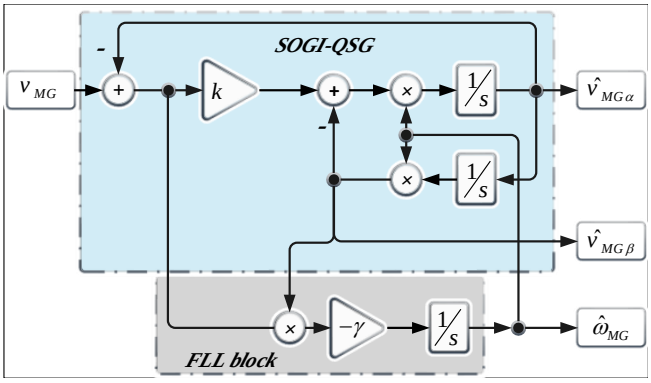

Figure 4: SOGI-FLL general structure.

where $\dot{v}_{MG}$ is the first derivative of the input voltage, $\dot{\hat{v}}_{MG\alpha}$ and $\ddot{\hat{v}}_{MG\alpha}$, are the first and the second derivatives of the estimated direct component $\hat{v}_{MG\alpha}$, respectively.

The representation of the input voltage and the direct component voltage in the phasor domain is illustrated in Fig. 5.

Accordingly, the expressions of v_{MG}, $\dot{v}_{MG}$, $\hat{v}_{MG\alpha}$, $\dot{\hat{v}}_{MG\alpha}$ and $\ddot{\hat{v}}_{MG\alpha}$ as a function of its synchronous reference frame components in the phasor domain, under frequency condition (i.e., $\hat{\omega}_{MG} = \omega_{MG}$), can be given by:

$$\begin{aligned}
\bar{v}_{MG} &= (v_{MG-d} + jv_{MG-q})\, e^{j\theta} \\
\dot{\bar{v}}_{MG} &= [\dot{v}_{MG-d} + j\dot{v}_{MG-q} + j\omega_{MG}\,(v_{MG-d} + jv_{MG-q})]\, e^{j\theta} \\
\bar{\hat{v}}_{MG\alpha} &= (\hat{v}_{MG\alpha-d} + j\hat{v}_{MG\alpha-q})\, e^{j\theta} \\
\dot{\bar{\hat{v}}}_{MG\alpha} &= \left[\dot{\hat{v}}_{MG\alpha-d} + j\dot{\hat{v}}_{MG\alpha-q} + j\omega_{MG}\,(\hat{v}_{MG\alpha-d} + j\hat{v}_{MG\alpha-q})\right] e^{j\theta} \\
\ddot{\bar{\hat{v}}}_{MG\alpha} &= \left[\ddot{\hat{v}}_{MG\alpha-d} + j\ddot{\hat{v}}_{MG\alpha-q} + 2\times j\omega_{MG}\left(\dot{\hat{v}}_{MG\alpha-d} + j\dot{\hat{v}}_{MG\alpha-q}\right) - \omega_{MG}^2\,(\hat{v}_{MG\alpha-d} + j\hat{v}_{MG\alpha-q})\right] e^{j\theta}
\end{aligned} \tag{11}$$

where j denotes the imaginary number and θ is the phase angle between the rotating and fixed frames.

By substituting Eq. (11) into Eq. (10), and after some mathematical manipulation, the expressions of $\hat{v}_{MG\alpha-d}$ and $\hat{v}_{MG\alpha-q}$ voltages as a function of the input voltage dq components (v_{MG-d}, v_{MG-q}), in the s-domain can be obtained as follows:

$$\begin{bmatrix} \hat{v}_{MG\alpha-d} \\ \hat{v}_{MG\alpha-q} \end{bmatrix} = k\omega_{MG} \frac{\begin{bmatrix} A & B \\ -B & A \end{bmatrix}}{\left(s^2 + k\omega_{MG}s\right)^2 + \left(k\omega_{MG}^2 + 2\omega_{MG}s\right)^2} \begin{bmatrix} v_{MG-d} \\ v_{MG-q} \end{bmatrix} \tag{12}$$

where:

$$\begin{cases} A = s^3 + k\omega_{MG}s^2 + 2\omega_{MG}^2 s + k\omega_{MG}^3 \\ B = \omega_{MG}s^2 \end{cases}$$

By proposing v_{MG} as a reference in the rotating reference frame, hence, $v_{MG-d} = E_{MG}$, $v_{MG-q} = 0$, $\hat{v}_{MG\alpha-d} = \hat{E}_{MG}$ and $\hat{v}_{MG\alpha-q} = 0$, Eq. (12) becomes:

$$\hat{E}_{MG} = k\omega_{MG} \frac{\left[s^3 + k\omega_{MG}s^2 + 2\omega_{MG}^2 s + k\omega_{MG}^3\right]}{\left[s\,(s + k\omega_{MG})\right]^2 + \left[\omega_{MG}\,(2s + k\omega_{MG})\right]^2} E_{MG} \tag{13}$$

This transfer function describes the amplitude estimation dynamics of the SOGI-FLL.

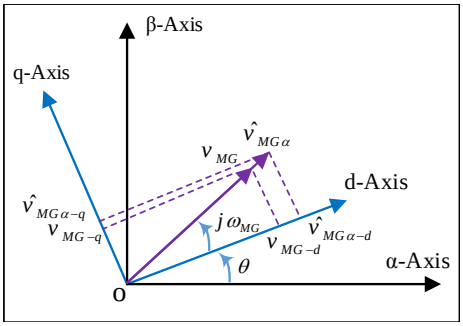

Figure 5: Phasor representation of the input v_{MG} and the direct component $\hat{v}_{MG\alpha}$ voltages

The obtained actual transfer function, given by Eq. (13), is very complex, thus, for the sake of simplicity this transfer function can be approximated as a first-order transfer function based on the analysis of its poles. Hence, the poles of the fourth-order transfer function given by Eq. (13), for $-2 \leqslant k \leqslant 2$, can be expressed as follow:

$$\begin{cases} P_{1,2} = -\frac{k\omega_{MG}}{2} - J\omega_{MG}\left(1 \pm \sqrt{1-\left(\frac{k}{2}\right)^2}\right) \\ P_{3,4} = -\frac{k\omega_{MG}}{2} + J\omega_{MG}\left(1 \pm \sqrt{1-\left(\frac{k}{2}\right)^2}\right) \end{cases} \tag{14}$$

It can be noticed from these expressions that P_2 and P_4, which have the lowest imaginary part, are the dominant poles. Thus, these poles are taken for the reduced second-order transfer function. Then, the multiplication of the dominant poles ($P2 \times P4$) gives a real pole, which is the pole of the simple first-order transfer function. In addition, by setting the steady-state gain to be the same, the simple model that describes the amplitude estimation dynamics of the SOGI-FLL is given by:

$$\hat{E}_{MG} = \frac{k\omega_{MG}/2}{\left(s + k\omega_{MG}/2\right)} E_{MG} \tag{15}$$

To verify the accuracy of the obtained frequency and amplitude models given by Eqs. (8), (13) and (15), a simulation study using MATLAB/Simulink environment is conducted. In this simulation study, the estimated frequency and amplitude by the SOGI-FLL are compared with the ones predicted by their models for step changes in the input frequency and amplitude, respectively. The transient responses of the frequency estimate for two different values of the FLL gain (Γ) are illustrated in Fig. 6 (a), while, Fig. 6 (b) shows the amplitude estimate transient responses for two distinct values of the SOGI-FLL parameter k. From these figures, it can be seen that the obtained models can predict accurately the average dynamic behavior of SOGI-FLL regarding frequency and amplitude estimation.

Consequently, the obtained models are useful to be introduced in the restoration control loops for the estimation of microgrid voltage amplitude and frequency.

3.2. Modeling of the frequency and amplitude restoration loops

This subsection presents in details the dynamical modeling of the frequency and amplitude restoration control loops.

3.2.1. Voltage control loop

The block diagram of the voltage control model based on the derived simple model, which describes the amplitude estimation dynamics of the SOGI-FLL, is shown in Fig. 7. This block diagram is composed of: a droop control model, an IP-type controller followed by a communication line delay (G_d), and the derived simple model (H_{SOGI}) used to extract the microgrid amplitude.

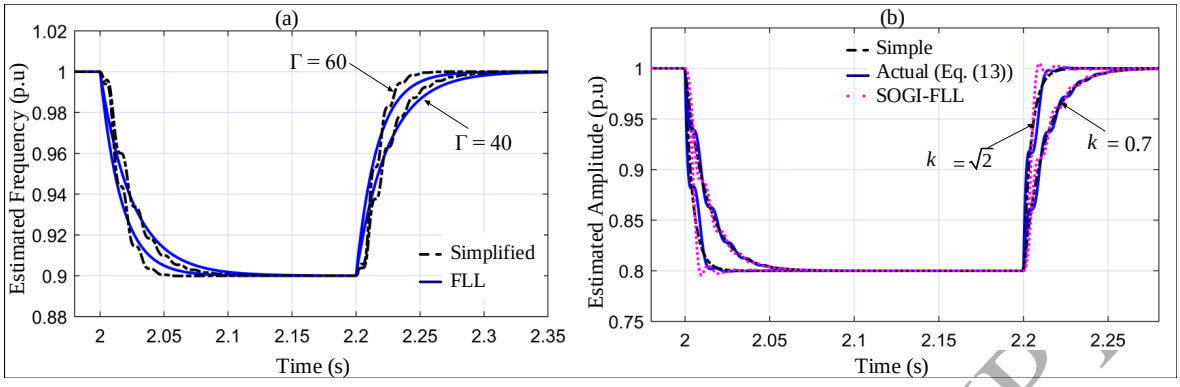

Figure 6: Transient responses of: (a) the SOGI-FLL and its simplified model (Eq. (8)) for $\Gamma = 40s^{-1}$ and $\Gamma = 60s^{-1}$, (b) The SOGI-FLL, and its actual model and simple model (Eq. (15)) for $k = 0.7$ and $k = \sqrt{2}$

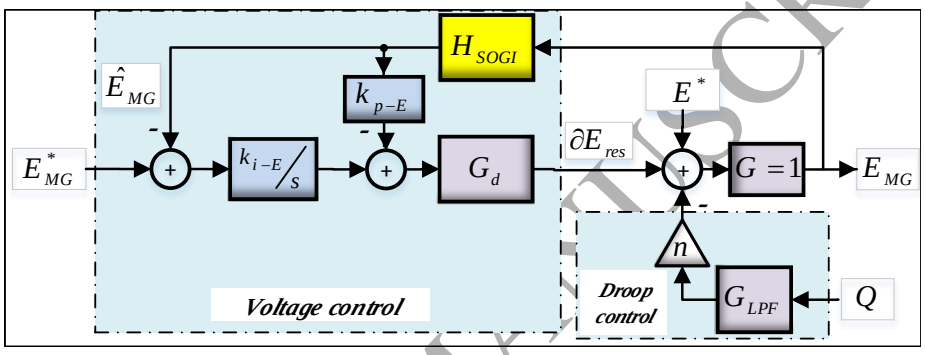

Figure 7: Block diagram of the voltage secondary control model.

According to Fig. 7, the closed loop transfer function of the voltage restoration control can be obtained as follows:

$$E_{MG} = \frac{\left[k_{i-E}/s\right] G_d(s)}{1 + G_{PI-E}(s) H_{SOGI}(s) G_d(s)} E^*_{MG} - \frac{nG_{LPF}(s)}{1 + G_{PI-E}(s) G_d(s) H_{SOGI}(s)} Q \tag{16}$$

where the transfer functions are given below:

$$G_{PI-E}(s) = \frac{k_{p-E}s + k_{i-E}}{s} \tag{17}$$

$$G_d(s) = \frac{1}{\tau s + 1} \tag{18}$$

$$G_{LPF}(s) = \frac{\omega_f}{s + \omega_f} \tag{19}$$

$$H_{SOGI}(s) = \frac{k\omega_{MG}/2}{\left(s + k\omega_{MG}/2\right)} \tag{20}$$

where τ is the time delay of the communication link, and G_{LPF} is a low pass filter considered for reactive power calculation with a cutoff frequency $\omega_f = 2\pi \times 20$.

Substituting Eqs. (17) to (20) into Eq. (16), the complete mathematical form of the voltage control model

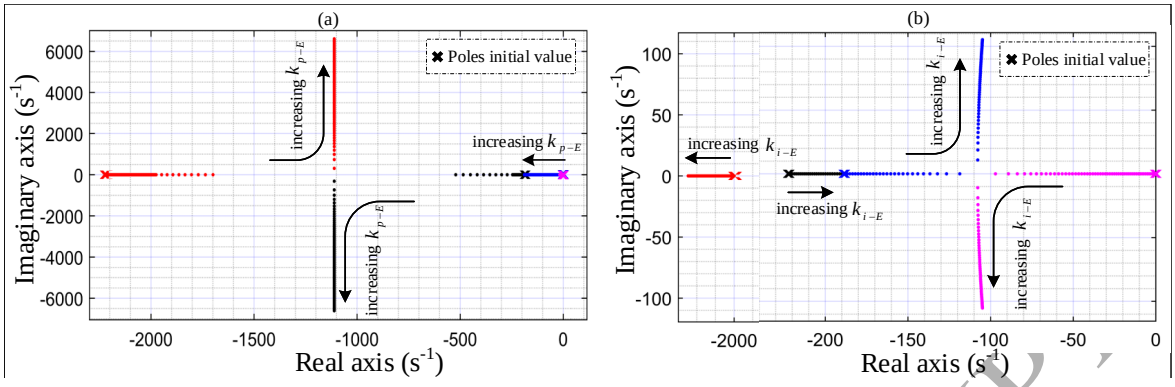

Figure 8: Root-Locus plots for: (a) $0.0001 \leqslant k_{i-E} \leqslant 100$ and $k_{p-E} = 0.01$, and (b) $-1 \leqslant k_{p-E} \leqslant 100$ and $k_{i-E} = 1.5$.

can be expressed as follows:

$$E_{MG} = \frac{\left(k_{i-E}s^2 + ak_{i-E}s + c\right)}{s^3 + as^2 + bs + c}\left[\frac{1}{s\left(\tau s + 1\right)}\right]E^*_{MG} - \frac{n\left(s^2 + as + c/k_{i-E}\right)}{s^3 + as^2 + bs + c}\left[\frac{\omega_f}{s + \omega_f}\right]Q \tag{21}$$

with the following parameters

$$a = \frac{k\omega_{MG}}{2} + \frac{1}{\tau}$$

$$b = \frac{k\omega_{MG}}{2\tau}\left(1 + k_{p-E}\right)$$

$$c = k_{i-E}\frac{k\omega_{MG}}{2\tau}$$

The obtained amplitude control model is used to analyze the stability of the MG system for control parameters variation. Fig. 8 (a) and (b) depict a series of root-locus diagrams, showing the evaluation of the characteristic equation eigenvalues for k_{p-E} and k_{i-E} variation, respectively. From these figures, it is clearly shown that the system eigenvalues move toward an unstable region when the controller proportional and integral terms increase. Hence, this increases the system oscillations and consequently, the microgrid goes to instability.

3.2.2. Frequency control loop

Fig. 9 shows the block diagram of the frequency control model based on the FLL linearized model. This block consists of: a droop control model, the FLL model (H_{FLL}) used to estimate the microgrid frequency, an IP-type controller and a communication line delay (G_d). According to this figure, the closed loop transfer function that describes the frequency restoration dynamics can be derived as follows:

$$\omega_{MG} = \frac{\left[k_{i-f}/_s\right]G_d\left(s\right)}{1 + G_{PI-f}\left(s\right)G_d\left(s\right)H_{FLL}\left(s\right)}\omega^*_{MG} - \frac{mG_{LPF}\left(s\right)}{1 + G_{PI-f}\left(s\right)G_d\left(s\right)H_{FLL}\left(s\right)}P \tag{22}$$

where the transfer functions H_{FLL} and G_{PI-f} are given by:

$$G_{PI-f}\left(s\right) = \frac{k_{p-f}s + k_{i-f}}{s} \tag{23}$$

$$H_{FLL}\left(s\right) = \frac{\Gamma}{s + \Gamma} \tag{24}$$

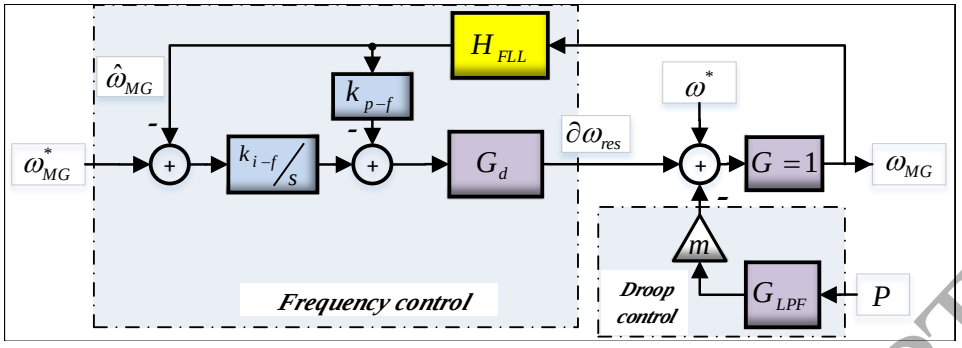

Figure 9: Block diagram of the frequency secondary control model.

By substituting the expression of these transfer functions into Eq. (22), the small signal model of the frequency restoration control can be obtained as follows:

$$\omega_{MG} = \frac{\left(k_{i-f}s^2 + ak_{i-f}s + c\right)}{s^3 + as^2 + bs + c}\left[\frac{1}{s\left(\tau s + 1\right)}\right]\omega^*_{MG} - \frac{m\left(s^2 + as + c/k_{i-f}\right)}{s^3 + as^2 + bs + c}\left[\frac{\omega_f}{s + \omega_f}\right]P \tag{25}$$

with the following parameters:

$$a = \Gamma + \frac{1}{\tau}$$
$$b = \frac{\Gamma}{\tau}\left(1 + k_{p-f}\right)$$
$$c = k_{i-f}\frac{\Gamma}{\tau}$$

The stability analysis of the microgrid system is performed based on the extracted frequency model. The trajectory of the characteristic polynomial eigenvalues of this model as a function of the frequency control parameters, k_{p-f} and k_{i-f}, is presented in Fig. 10 (a) and (b). These figures show that when k_{p-f} and k_{i-f} increase the two dominant eigenvalues of the system move toward unstable region, hence, leads the microgrid to instability issues.

3.3. Tuning Control Parameters

To properly select the parameters of the frequency and amplitude restoration control, the following analysis based on the obtained models is developed. According to Eq. (21) and Eq. (25), the transfer functions relating the actual amplitude and frequency to the desired ones can be derived as follow:

$$E_{MG} = \frac{\left(k_{i-E}s^2 + ak_{i-E}s + c\right)}{s^3 + as^2 + bs + c}\left[\frac{1}{s\left(\tau s + 1\right)}\right]E^*_{MG} \tag{26}$$

$$\omega_{MG} = \frac{\left(k_{i-f}s^2 + ak_{i-f}s + c\right)}{s^3 + as^2 + bs + c}\left[\frac{1}{s\left(\tau s + 1\right)}\right]\omega^*_{MG} \tag{27}$$

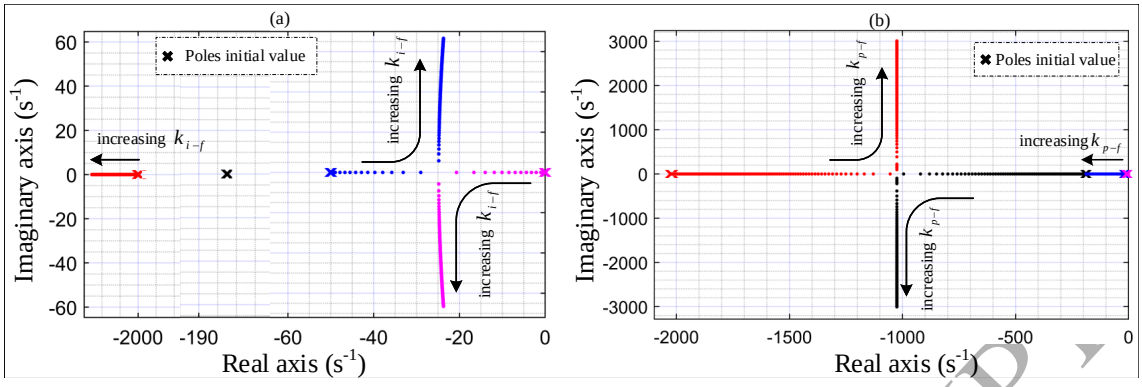

Figure 10: Root-Locus plots for: (a) $0.0001 \leqslant k_{i-f} \leqslant 100$ and $k_{p-f} = 0.01$, and (b) $-0.5 \leqslant k_{p-f} \leqslant 100$ and $k_{i-E} = 2.6$.

By assuming that the time delay is negligible regarding SOGI-FLL estimation time and that the perturbation amount of the droop model is also negligible, hence Eq. (26) and Eq. (27) becomes:

$$E_{MG} = \frac{k_{i-E}\frac{k\omega_{MG}}{2}}{s^2 + \frac{k\omega_{MG}}{2}\left(1 + k_{p-E}\right)s + k_{i-E}\frac{k\omega_{MG}}{2}} E^*_{MG} \tag{28}$$

$$\omega_{MG} = \frac{\Gamma k_{i-f}}{s^2 + \Gamma\left(1 + k_{p-f}\right)s + k_{i-f}\Gamma}\omega^*_{MG} \tag{29}$$

The characteristic polynomials of these transfer functions are:

$$s^2 + \underbrace{\frac{k\omega_{MG}}{2}\left(1 + k_{p-E}\right)}_{2\zeta_E\omega_{n-E}}s + \underbrace{k_{i-E}\frac{k\omega_{MG}}{2}}_{\omega^2_{n-E}} = 0 \tag{30}$$

$$s^2 + \underbrace{\frac{k\omega_{MG}}{2}\left(1 + k_{p-f}\right)}_{2\zeta_f\omega_{n-f}}s + \underbrace{k_{i-f}\frac{k\omega_{MG}}{2}}_{\omega^2_{n-f}} = 0 \tag{31}$$

where ζ and ω_n stand for the damping factor and the natural frequency, respectively.
Accordingly, the expressions of the proportional and integral gains of both amplitude and frequency controllers can be expressed as follow:

$$\begin{cases} k_{p-E} = \frac{4\zeta_E\omega_{n-E}}{k\omega_{MG}} - 1 \\ k_{i-E} = \frac{2\omega^2_{n-E}}{k\omega_{MG}} \end{cases} \tag{32}$$

$$\begin{cases} k_{p-f} = \frac{2\zeta_f\omega_{n-f}}{\Gamma} - 1 \\ k_{i-f} = \frac{2\omega^2_n}{\Gamma} \end{cases} \tag{33}$$

Based on the control design concept for deadbeat response proposed in [35], and by selecting proper value of the damping factor ζ that can ensure, in an optimum way, a tradeoff between overshoot and settling time, the corresponding natural frequency can be determinate relatively to the desired settling time of the control response. Once ζ and ω_n are chosen, the controller parameters can be computed using Eqs. (32) and (33). It is worth mentioning that the value of the damping factor ζ is chosen according to the analysis based on root-locus plots given in Figs. 8 and 10 and, then, verified according to the transient response of the obtained models.

In order to evaluate the robustness of the designed frequency and amplitude controllers for system parameters variation and under load disturbances, a simulation study in MATLAB/Simulink is carried out. In

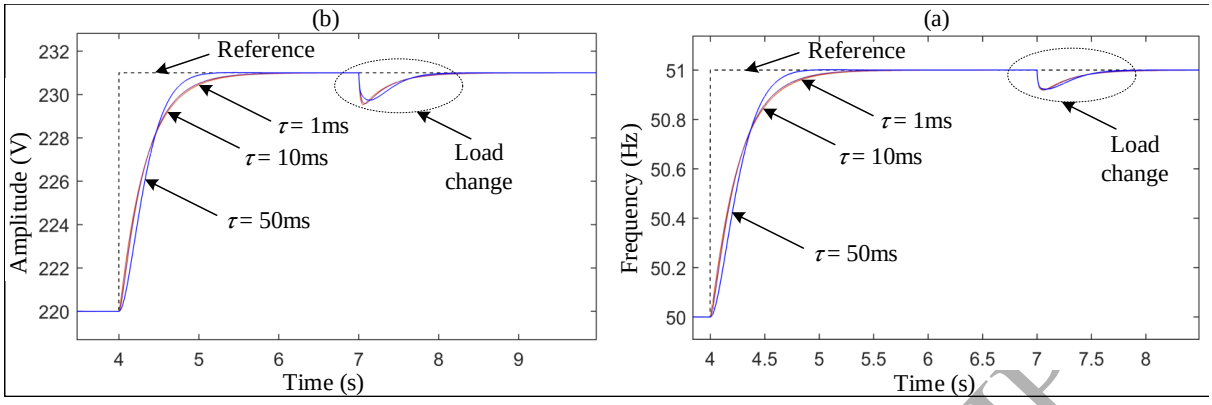

Figure 11: Transient responses of the secondary control models for: (a) frequency and (b) amplitude restoration, with three different values of the time delay (τ).

this study, the transient performances of the obtained secondary control models in response to step changes in the frequency and amplitude references and active and reactive powers are evaluated, considering three distinct values for the time delay (τ). The obtained results are depicted in Fig. 11 (a) and (b), and shown the transient response of the frequency and amplitude restoration control, respectively. It can be observed that the proposed control approach is robust against time delay variation and load changes, as amplitude and frequency of the MG are properly restored.

3.4. Synchronization control loop

In this subsection, the modeling and control design of the synchronization control loop are presented. The synchronization control scheme is given in Fig. 2, and it is included within the scope of the secondary control layer. According to Fig. 2, the expression of the proposed synchronization controller can be given by:

$$\partial\omega_{\text{syn}} = k_{p-\phi}\left(\phi^* - \phi\right) \tag{34}$$

where $k_{p-\phi}$ is the proportional gain term of the synchronization controller, ϕ^* is the phase angle reference, which set to zero, and ϕ is the phase difference between the MG and the main gird.

Actually, the expression of the phase angle difference ϕ can be obtained based on the cross product mathematical formulas.

According to the first formula, the cross product of the microgrid and the main grid voltages can be defined by [36]:

$$\|\vec{v}_g \times \vec{v}_{MG}\| = \hat{V}_g \hat{E}_{MG} \sin\left(\phi\right) \tag{35}$$

where $\hat{V}_g$ is the estimated voltage amplitude of the main grid.

The second formula of the cross product in the stationary reference frame can be expressed as:

$$\|\vec{v}_g \wedge \vec{v}_{MG}\| = \hat{v}_{g\alpha}\hat{v}_{MG\beta} - \hat{v}_{MG\alpha}\hat{v}_{g\beta} \tag{36}$$

where $\hat{v}_{MG\alpha\beta}$ and $\hat{v}_{g\alpha\beta}$ are the extracted orthogonal components of the microgrid and the main grid voltages. Subtracting Eq. (35) from Eq. (36), and considering small phase angle variation, i.e., $\sin(\phi) \simeq (\phi)$ the expression of the phase angle difference can be found as follows:

$$\phi = \frac{\hat{v}_{g\alpha}\hat{v}_{MG\beta} - \hat{v}_{MG\alpha}\hat{v}_{g\beta}}{\hat{V}_g \hat{E}_{MG}} = \frac{\hat{v}_{g\alpha}\hat{v}_{MG\beta} - \hat{v}_{MG\alpha}\hat{v}_{g\beta}}{\hat{E}^2_{MG}} \tag{37}$$

Consequently, Eq. (34) becomes:

$$\partial\omega_{\text{syn}} = -k_{p-\phi}\frac{\hat{v}_{g\alpha}\hat{v}_{MG\beta} - \hat{v}_{MG\alpha}\hat{v}_{g\beta}}{\hat{E}^2_{MG}} \tag{38}$$

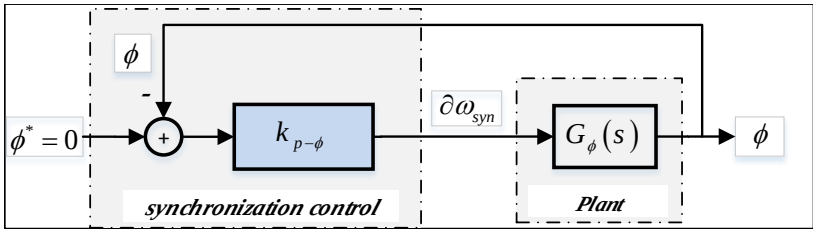

Figure 12: Block diagram of the Synchronization feedback control.

To adjust the parameter $k_{p-\phi}$ of the synchronization controller, a model is developed as can be seen in Fig. 12. This figure depicts the block diagram of the phase angle control, which includes the plant model ($G_\phi(s)$) and the synchronization control model. According to this figure, the closed loop transfer function of the phase angle control can be derived as follows:

$$\phi = \frac{k_{p-\phi} G_\phi(s)}{1 + k_{p-\phi} G_\phi(s)} \phi^* \tag{39}$$

where the expression of the plant model $G_\phi(s)$ is given by:

$$G_\phi(s) = \frac{1}{s} \tag{40}$$

Substituting Eq. (40) into Eq. (39), the closed loop model of the phase angle control can be obtained as follows:

$$\phi = \frac{k_{p-\phi}}{s + k_{p-\phi}} \phi^* \tag{41}$$

By applying the first-order control design concept to the transfer function given by Eq. (41), the proportional gain $k_{p-\phi}$ can be calculated using the following expression:

$$k_{p-\phi} = -\frac{1}{T_s} \ln(0.02) \tag{42}$$

where T_s is the desired settling time.

4. Numerical simulation

A simulation study, under MATLAB/Sim Power System environment, is carried out in order to assess the effectiveness and the robustness of the proposed secondary control approach. Based on the structure given in Fig. 2, a system test of an islanded microgrid is built up. The constructed microgrid consists of two DG units with the same power rate (2.5 kW), feeding a local inductive load (40 Ω, 1 mH). The secondary control parameters are selected according to the presented tuning process so that its response is ten times slower than the primary control. The parameters taken in the simulation study are reported in Table 1.

Table 1: Power stage and control parameters

Parameter	Symbol	Unit	Value
Inverters power stage			
Nominal voltage (RMS)	E^* (RMS)	V	220
Nominal frequency	$\omega^*/2\pi$	Hz	50
DC bus voltage	V_{dc}	V	450
Loads	R_L, L_L	Ω, mH	40, 1
Filter capacitor	C_{f1}, C_{f2}	μF	26
Filter inductor	$r_{1,2}, L_{f1,2}$	Ω, mH	0.5, 2.5
DG1 line impedance	L_{l1}	mH	0.9
DG2 line impedance	L_{l2}	mH	1.2
SOGI-FLL scheme			
SOGI gain	k	-	0.7
FLL gain	Γ	s^{-1}	40
Primary control			
Frequency-droop gain	m	$W/rad.s$	0.0003
Amplitude-droop gain	n	VAr/V	0.003
Virtual impedance	L_v	mH	4
Secondary control			
Voltage proportional gain	k_{p-E}	-	-0.45
Voltage integral gain	k_{i-E}	s^{-1}	1.57
Frequency proportional gain	k_{p-f}	-	-0.22
Frequency integral gain	k_{i-f}	s^{-1}	2.67
Synchronization gain	$k_{p-\phi}$	s^{-1}	0.76
Communication delay time	τ	ms	0.5

The following case studies are considered:

- Case 1: This case aims to evaluate the performance of the frequency and amplitude restoration control in the presence of frequent load changes. To this end, the microgrid begins with no-load operating condition, and next DG units (1 and 2) start to feed a common inductive load at t = 1 s, while only the primary control is running. At t = 2 s, the frequency and amplitude restoration control are activated, then a load change is realized, by disconnecting and reconnecting a resistive load (40 Ω) from/to the microgrid at t = 5 s and t = 7.5 s, respectively.

- Case 2: The aim of this case study is testing the proposed restoration controller performance under DG disconnection operating condition. For this purpose, a sudden disconnection of the inverter #2 from the microgrid is programmed at t = 5 s, and only inverter #1 remain supplying the common load, where the same scenarios; as the first case by starting with no-load and next enabling the primary and secondary controls with an inductive load; are considered.

- Case 3: This case study analyses the performances of the synchronization controller. So, this controller is enabled at t = 5 s, to synchronize the microgrid with the main utility grid (50 Hz and 220 V).

Fig. 13 shows the transient responses of the frequency, amplitude, and active and reactive powers, of DG1, DG2 and the microgrid (or common load bus (CLB)), for the first case study. It can be observed that at no-load operating condition, the frequency and the amplitude of each DG unit and at the CLB are at their nominal values. Then, when a load is suddenly connected; while the primary control is running; they drooped with the same amounts in order to share the active and reactive powers of the load, which is also demonstrated. When the restoration process is enabled (at t = 2 s), the frequency and amplitude static deviations produced by the droop control are removed. Notice that the frequency and voltage inside the microgrid are seamlessly restored to the nominal values, i.e., 50 Hz and 311 V. In addition, as it is shown, the proposed secondary

controller ensures a smooth frequency and voltage recovery when a load change suddenly occurs (at t = 5 s and 7.5 s), and the active and reactive powers-sharing is still guaranteed. We note that the proposed controller provides good transient responses in respect to the desired predefined performances; settling time around 1 s and without overshoots.

The obtained results demonstrating the performances of the proposed restoration control for case 2 are given in Fig. 14. It can be seen that, when the DG2 is disconnected from the microgrid (at t = 5 s), the designed controllers restore successfully the frequency and amplitude of the microgrid, formed only by DG1, to their nominal values. Note that the settling time of the frequency and voltage transient responses is about 1 s. In addition, it can be seen that the DG2 variables are set to the nominal values. It is worth mentioning that the small difference between the voltage amplitude of DG1 and the nominal value is due to the voltage amplitude of the line impedance.

Fig. 15 illustrates the obtained results for case 3. It can be observed that, when the synchronization process is enabled (at t = 5 s), the phase angle difference between the microgrid and the main utility grid moves toward zero. Also, the frequency and amplitude of the DG units and CLB are fixed to the grid set points. While the active power remains constant during the synchronization process. We notice that the settling time of the synchronization transient response is around 5 s.

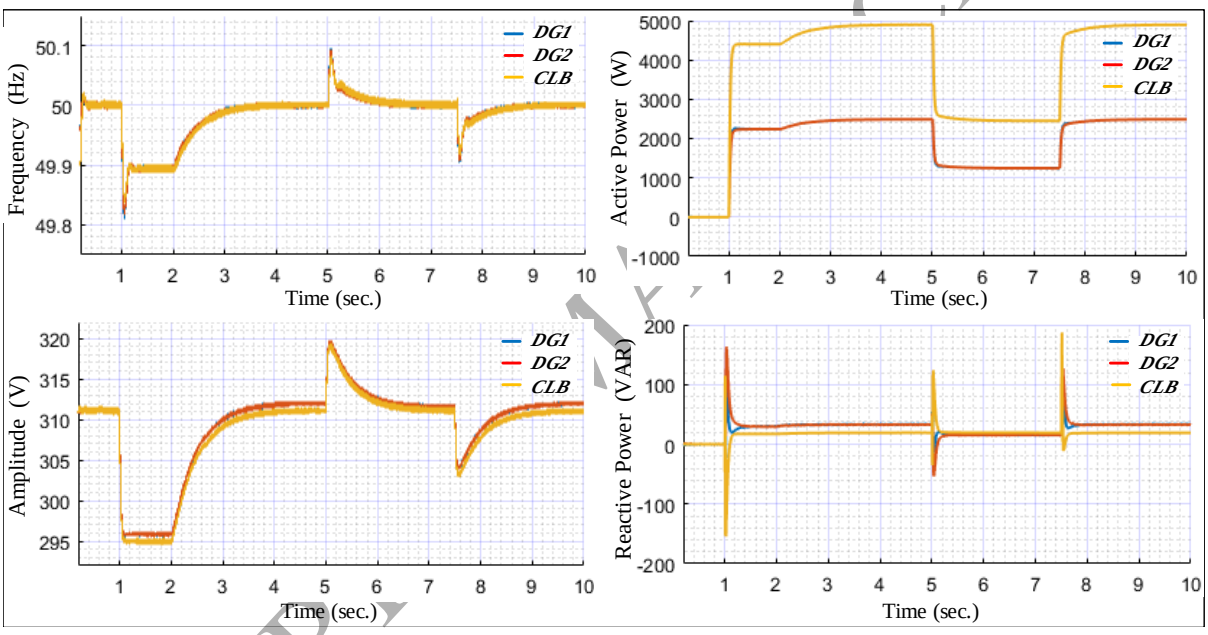

Figure 13: Obtained results in response to case 1

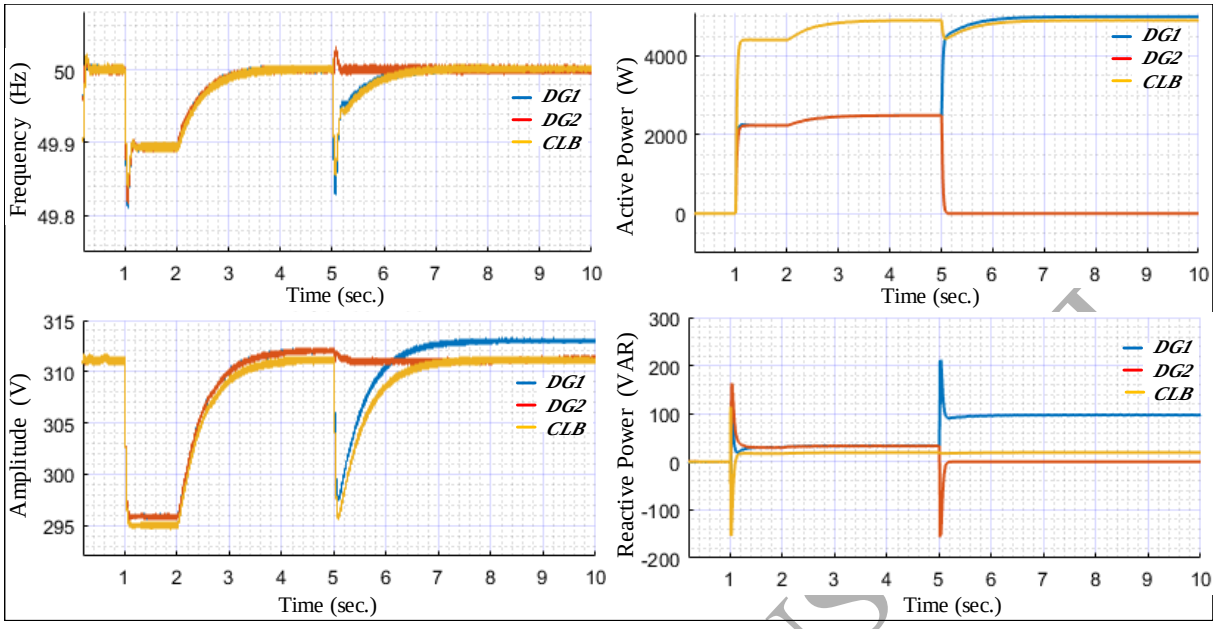

Figure 14: Obtained results in response to case 2

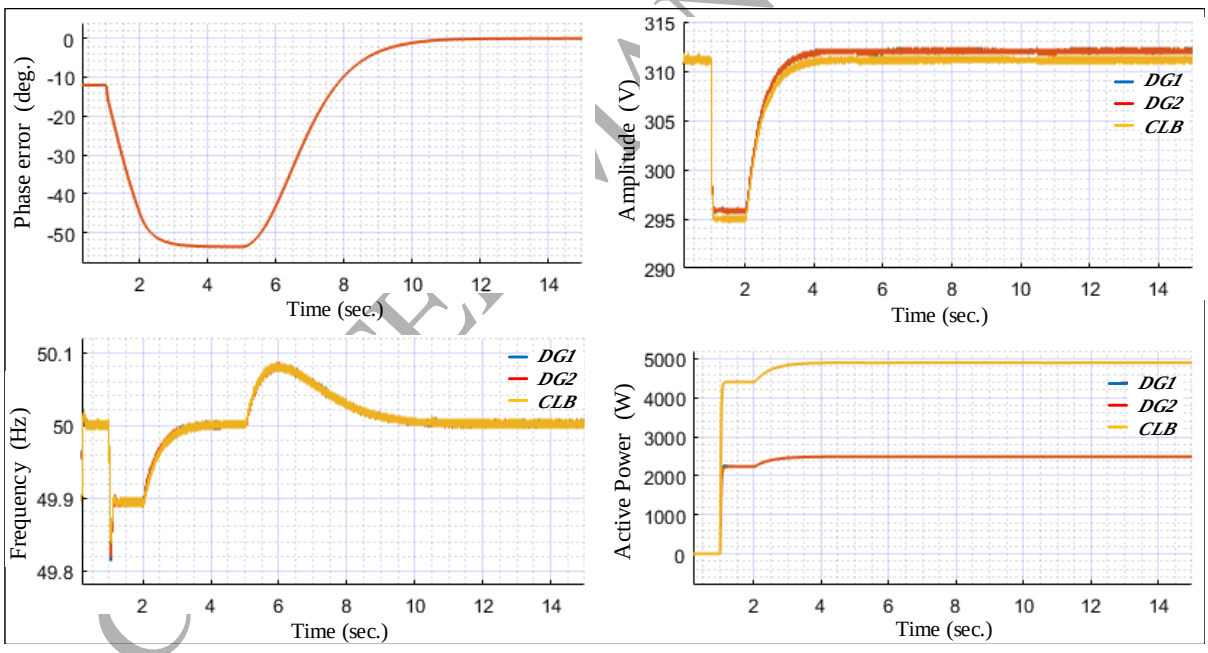

Figure 15: Obtained results in response to case 3.

5. Experimental results

In order to evaluate the performance of the proposed secondary control approach, an experimental set-up is built as shown in Fig. 16. This experimental set-up is similar to the structure presented in Fig. 2, where two single-phase full-bridge VSIs with LC filter are connected in parallel, forming an islanded microgrid

Table 2: Experimental parameters

Parameter	Symbol	Unit	Value
Inverters power stage			
Nominal voltage (RMS)	E^* (RMS)	V	30
Nominal frequency	$\omega^*/2\pi$	Hz	50
DC bus voltage	V_{dc}	V	60
Loads	R_L	Ω	8
Filter capacitor	C_{f1}, C_{f2}	μF	16, 18
DG1 Filter inductor	r_1, L_{f1}	Ω, mH	0.3, 2.7
DG2 Filter inductor	$r_2 L_{f1}$	Ω, mH	0.5, 2.6
DG1 line impedance	L_{l1}	mH	0.8
DG2 line impedance	L_{l2}	mH	0.5
SOGI-FLL scheme			
SOGI gain	k	-	0.7
FLL gain	Γ	s^{-1}	40
Primary control			
Frequency-droop gain	m	$W/rad.s$	0.003
Amplitude-droop gain	n	VAr/V	0.03
Virtual impedance	L_v	mH	2
Secondary control			
Voltage proportional gain	k_{p-E}	-	-0.69
Voltage integral gain	k_{i-E}	s^{-1}	0.49
Frequency proportional gain	k_{p-f}	-	-0.71
Frequency integral gain	k_{i-f}	s^{-1}	0.58
Synchronization gain	$k_{p-\phi}$	s^{-1}	0.35
Communication delay time	τ	ms	1

with a power rate of 0.1 kW. The primary control of each DG unit and the designed secondary control are implemented in separate ARM Cortex microcontroller (STM32F407). RS232 (URAT) protocol is used to communicate between these microcontrollers for the aim of sending the produced control signals by the secondary controller toward the DGs local controllers. In addition, measurements sensors are used to provide the required voltages and currents to the ARM Cortex microcontrollers via signal conditioning circuits. For more details, the algorithms of the primary and secondary control, given in the upper part of Fig. 16, are programmed in MATLAB Simulink based STM32F4 Embedded Target and, then, the generated code using Embedded Coder are loaded into the STM32F4 board. The sampling frequencies of the primary and secondary controls are set to 10 kHz and 1 kHz, respectively. The power stage and the control parameters taken in this experiment are summarized in Table 2.

It is worth noting that the same cases as the simulation study are considered in the experimental test. However, these tests are carried out at different times and load values. In addition, the obtained results are extracted from ARM microcontrollers and plotted using MATLAB to provide better quality.

In the first experiment, before the secondary control for frequency and voltage restoration is enabled at t = 15 s, only the primary control was running. Next, at t = 25 s and t = 35 s, a resistive load of 8 Ω is suddenly disconnected and reconnected from/to the MG. Fig. 17 shows how the restoration control regulated the frequency and voltage deviation inside the DGs in response to this experiment test. From these figures, it can be seen that frequency and amplitude of both DGs voltage and at the CLB are seamlessly restored to their nominal values when the secondary control is enabled (at t = 15 s), and after load change as well (at t = 25 s and 35 s). In addition, it can be remarked that the settling time of frequency and amplitude transient response is around 5 s. Notice that the active and reactive powers-sharing between the DG units is still can be observed.

In the second experiment, after activating the secondary control at t = 15 s, the DG2 unit is suddenly

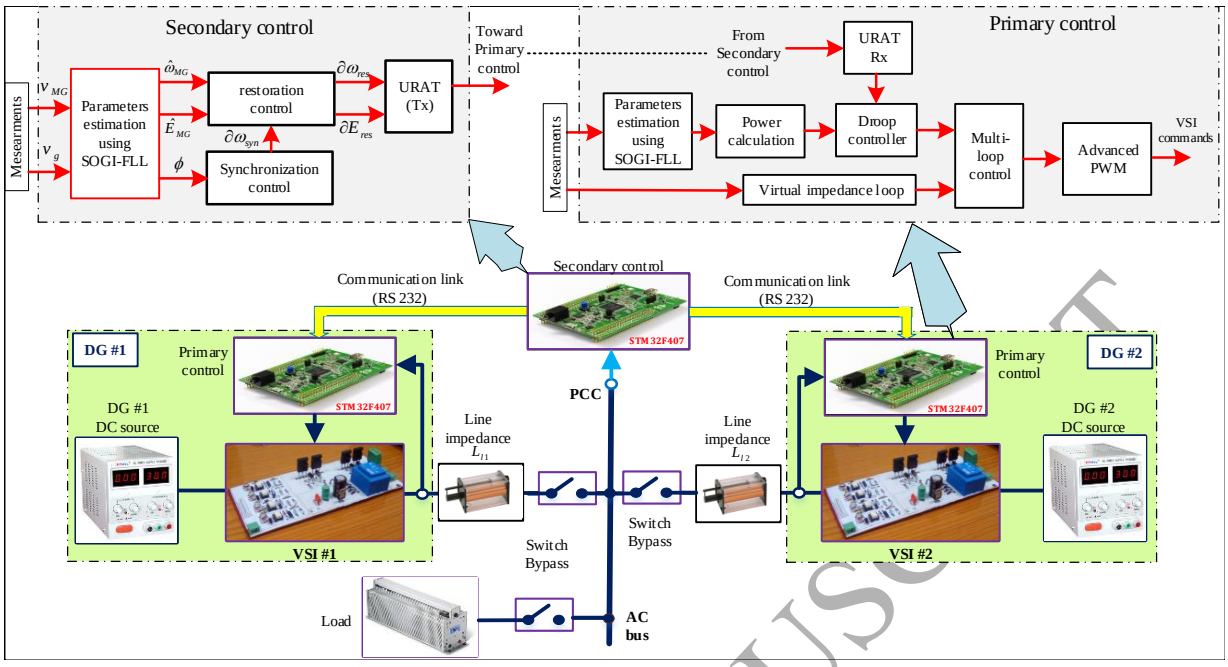

Figure 16: Block diagram of the experimental setup based on ARM Cortex μCs

disconnected from the MG at t = 26 s. Scopes of Fig. 18 show that the secondary controller is able to regulate successfully the frequency and amplitude to their rated values with the desired transient response (a settling time of 5 s and without overshoot). In the third experiment, the synchronization algorithm is introduced to synchronize the MG to the grid at t = 25 s, after enabling the secondary control at t = 15 s. Fig. 19 depicts the waveforms of the main grid and the MG voltages and their zooms for each scenario. It demonstrated that these voltages are accurately synchronized when the synchronization control is activated. In addition, it can be observed in Fig. 20, that the phase angle difference between the main grid and MG is matched to zero after a settling time of 10 s. Moreover, as shown, the voltage frequency and the amplitude of the CLB and the main grid are also matched. It is worth mentioning that the notches appearing in the figures of the experimental results are due to the power supplies fluctuations.

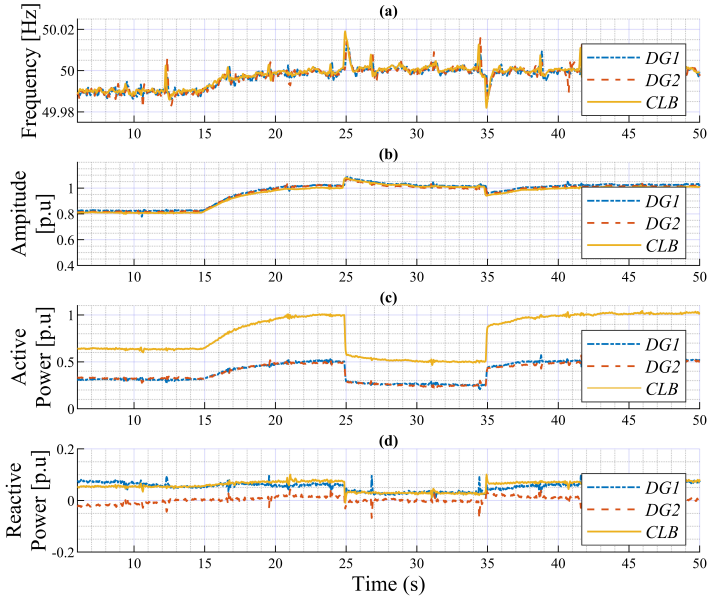

Figure 17: DGs and CLB: (a) frequency, (b) amplitude, (c) active power and (d) reactive power in response to test 1

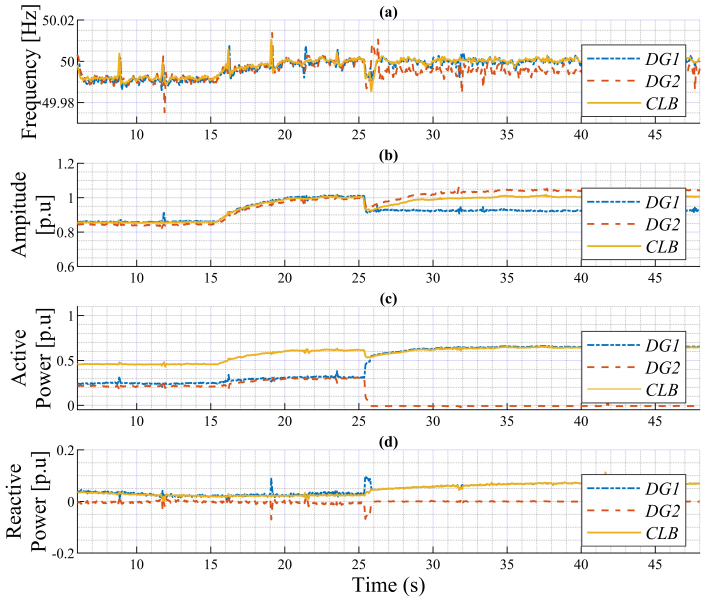

Figure 18: DGs and CLB: (a) frequency, (b) amplitude, (c) active power and (d) reactive power in response to test 2. DGs and CLB: (a) frequency, (b) amplitude, (c) active power and (d) reactive power in response to test 2

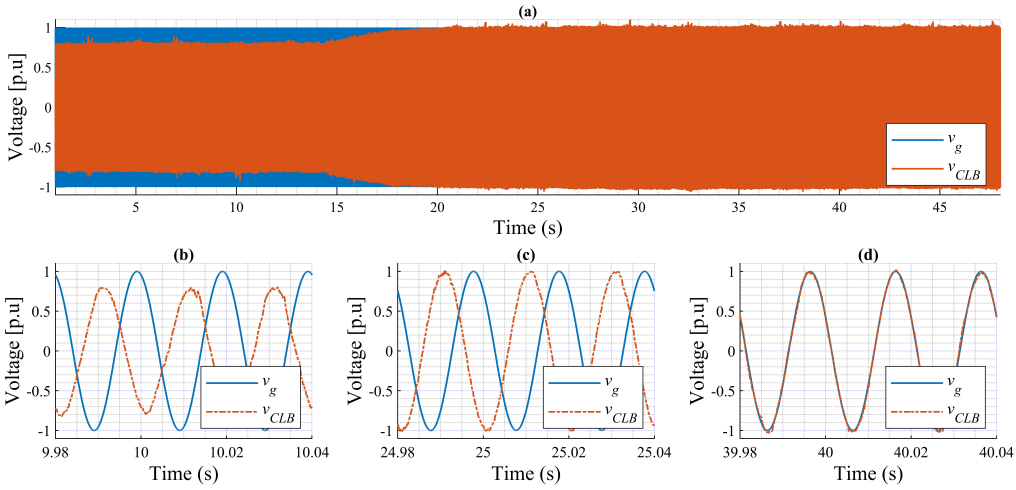

Figure 19: (a) Grid and CLB voltages and their zooms when: (b) only the primary control is running, (c) activating the restoration control, (d) enabling the synchronization control

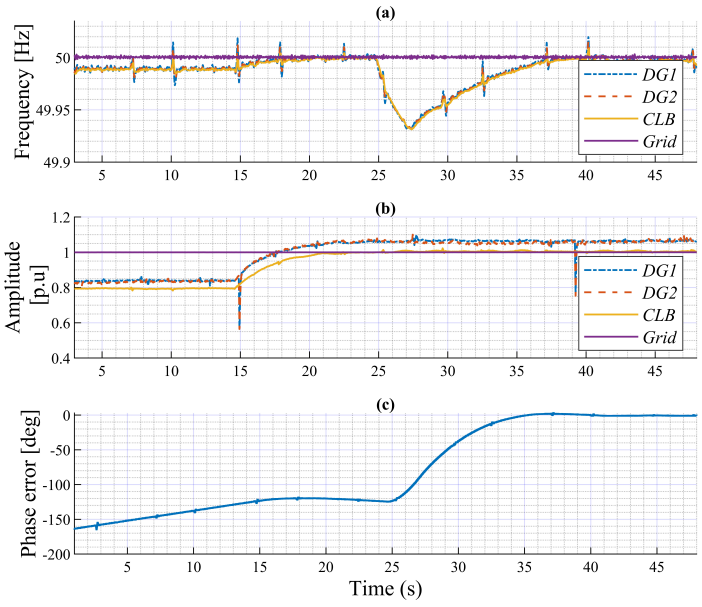

Figure 20: Experimental results: (a) frequency, (b) amplitude and (c) phase angle in response to test 3.

6. Conclusion

In this paper, a new approach to obtain accurate models of the secondary control for a single-phase microgrid was proposed. The proposed modeling approach exploits the dynamics of the SOGI-FLL scheme that have served to achieve precise stability analysis of the MG and the proper tuning of the secondary control parameters. The modeling and the design analysis of the synchronization control loop were also carried out, in this paper, in order to enable the transition from the islanded mode to grid-connected mode. The effectiveness

and the robustness of the proposed modeling approach were verified, on a hierarchical control including the designed secondary control for parallel VSIs supplying a common load, by simulation studies in MATLAB/ Sim power system and validated experimentally on ARM Cortex microcontrollers platform.

The obtained results from the simulation studies and the experimental tests have confirmed the robustness of the proposed control approach in keeping the frequency and voltage amplitude close to their nominal values under various disturbances. Additionally, the designed frequency and amplitude controllers have provided desired transient responses with the predefined performances. Transient responses with settling time around 1 s and 5 s, and without overshoot for simulation and practical results, respectively, were achieved. Furthermore, the synchronization algorithm has ensured a seamless transition from islanded mode to grid-connected mode, in which the settling times of the simulation and experimental transient responses were found as designed: 5 s and 10.

References

References

[1] J. G. De Matos, F. S. e Silva, L. A. d. S. Ribeiro, Power control in ac isolated microgrids with renewable energy sources and energy storage systems, IEEE Transactions on Industrial Electronics 62 (6) (2014) 3490–3498.

[2] D. Xu, Y. Dai, C. Yang, X. Yan, Adaptive fuzzy sliding mode command-filtered backstepping control for islanded pv microgrid with energy storage system, Journal of the Franklin Institute 356 (4) (2019) 1880–1898.

[3] M. Aryanezhad, Management and coordination of ltc, svr, shunt capacitor and energy storage with high pv penetration in power distribution system for voltage regulation and power loss minimization, International Journal of Electrical Power & Energy Systems 100 (2018) 178–192.

[4] A. Mehrizi-Sani, R. Iravani, Potential-function based control of a microgrid in islanded and grid-connected modes, IEEE Transactions on Power Systems 25 (4) (2010) 1883–1891.

[5] A. Bonfiglio, F. Delfino, A. Labella, D. Mestriner, F. Pampararo, R. Procopio, J. M. Guerrero, Modeling and experimental validation of an islanded no-inertia microgrid site, IEEE Transactions on Sustainable Energy 9 (4) (2018) 1812–1821.

[6] J. Rocabert, A. Luna, F. Blaabjerg, P. Rodriguez, Control of power converters in ac microgrids, IEEE transactions on power electronics 27 (11) (2012) 4734–4749.

[7] J. M. Guerrero, J. C. Vasquez, J. Matas, L. G. De Vicuña, M. Castilla, Hierarchical control of droop-controlled ac and dc microgridsa general approach toward standardization, IEEE Transactions on industrial electronics 58 (1) (2010) 158–172.

[8] J. M. Guerrero, M. Chandorkar, T.-L. Lee, P. C. Loh, Advanced control architectures for intelligent microgridspart i: Decentralized and hierarchical control, IEEE Transactions on Industrial Electronics 60 (4) (2012) 1254–1262.

[9] F. Delfino, G. Ferro, M. Robba, M. Rossi, An architecture for the optimal control of tertiary and secondary levels in small-size islanded microgrids, International Journal of Electrical Power & Energy Systems 103 (2018) 75–88.

[10] J. W. Simpson-Porco, F. Dörfler, F. Bullo, Synchronization and power sharing for droop-controlled inverters in islanded microgrids, Automatica 49 (9) (2013) 2603–2611.

[11] I. Ziouani, D. Boukhetala, A.-M. Darcherif, B. Amghar, I. E. Abbassi, A hierarchical control for flexible single-phase microgrid based on parallel vsis, in: 2017 6th International Conference on Systems and Control (ICSC), IEEE, 2017, pp. 178–182.

[12] A. Micallef, M. Apap, C. Spiteri-Staines, J. M. Guerrero, Single-phase microgrid with seamless transition capabilities between modes of operation, IEEE Transactions on Smart Grid 6 (6) (2015) 2736–2745.

[13] Z. Zhang, C. Dou, D. Yue, B. Zhang, W. Luo, A decentralized control method for frequency restoration and accurate reactive power sharing in islanded microgrids, Journal of the Franklin Institute 355 (17) (2018) 8874–8890.

[14] Z. Xiao, M. Zhu, Y. Huang, J. M. Guerrero, J. C. Vasquez, Coordinated primary and secondary frequency support between microgrid and weak grid, IEEE Transactions on Sustainable Energy (2018).

[15] F. Guo, C. Wen, J. Mao, Y.-D. Song, Distributed secondary voltage and frequency restoration control of droop-controlled inverter-based microgrids, IEEE Transactions on industrial Electronics 62 (7) (2014) 4355–4364.

[16] T. Dragičević, R. Heydari, F. Blaabjerg, Super-high bandwidth secondary control of ac microgrids, in: 2018 IEEE Applied Power Electronics Conference and Exposition (APEC), IEEE, 2018, pp. 3036–3042.

[17] G. Agundis-Tinajero, J. Segundo-Ramirez, N. Visairo-Cruz, M. Savaghebi, J. M. Guerrero, E. Barocio, Power flow modeling of islanded ac microgrids with hierarchical control, International Journal of Electrical Power & Energy Systems 105 (2019) 28–36.

[18] R. Neves, R. Machado, V. Oliveira, X. Wang, F. Blaabjerg, Multitask fuzzy secondary controller for ac microgrid operating in stand-alone and grid-tied mode, IEEE Transactions on Smart Grid (2018).

[19] Q. Shafiee, Č. Stefanović, T. Dragičević, P. Popovski, J. C. Vasquez, J. M. Guerrero, Robust networked control scheme for distributed secondary control of islanded microgrids, IEEE Transactions on Industrial Electronics 61 (10) (2013) 5363–5374.

[20] Y. Xu, H. Sun, W. Gu, Y. Xu, Z. Li, Optimal distributed control for secondary frequency and voltage regulation in an islanded microgrid, IEEE Transactions on Industrial Informatics 15 (1) (2018) 225–235.

[21] B. Wei, Y. Gui, A. Marzabal, S. Trujillo, J. M. Guerrero, J. Vasquez, Distributed average integral secondary control for modular ups systems based microgrids, IEEE Transactions on Power Electronics (2018).

[22] J. C. Vasquez, J. M. Guerrero, M. Savaghebi, J. Eloy-Garcia, R. Teodorescu, Modeling, analysis, and design of stationary-reference-frame droop-controlled parallel three-phase voltage source inverters, IEEE Transactions on industrial electronics 60 (4) (2012) 1271–1280.

[23] C. Ahumada, R. Cárdenas, D. Saez, J. M. Guerrero, Secondary control strategies for frequency restoration in islanded microgrids with consideration of communication delays, IEEE Transactions on Smart Grid 7 (3) (2015) 1430–1441.

[24] Q. Shafiee, J. M. Guerrero, J. C. Vasquez, Distributed secondary control for islanded microgridsa novel approach, IEEE Transactions on power electronics 29 (2) (2013) 1018–1031.

[25] R. Heydari, T. Dragicevic, F. Blaabjerg, High-bandwidth secondary voltage and frequency control of vsc-based ac microgrid, IEEE Transactions on Power Electronics (2019).

[26] A. D. Banadaki, F. D. Mohammadi, A. Feliachi, State space modeling of inverter based microgrids considering distributed secondary voltage control, in: 2017 North American Power Symposium (NAPS), IEEE, 2017, pp. 1–6.

[27] A. Micallef, M. Apap, C. Spiteri-Staines, J. M. Guerrero, J. C. Vasquez, Reactive power sharing and voltage harmonic distortion compensation of droop controlled single phase islanded microgrids, IEEE Transactions on Smart Grid 5 (3) (2014) 1149–1158.

[28] X. Zhou, L. Zhou, Y. Chen, Z. Shuai, J. M. Guerrero, A. Luo, W. Wu, L. Yang, Robust grid-current-feedback resonance suppression method for lcl-type grid-connected inverter connected to weak grid, IEEE Journal of Emerging and Selected Topics in Power Electronics 6 (4) (2018) 2126–2137.

[29] Y. Han, H. Li, P. Shen, E. A. A. Coelho, J. M. Guerrero, Review of active and reactive power sharing strategies in hierarchical controlled microgrids, IEEE Transactions on Power Electronics 32 (3) (2016) 2427–2451.

[30] W. Issa, F. Al-Naemi, G. Konstantopoulos, S. Sharkh, M. Abusara, Stability analysis and control of a microgrid against circulating power between parallel inverters, Energy Procedia 157 (2019) 1061–1070.

[31] Y. Yang, F. Blaabjerg, A new power calculation method for single-phase grid-connected systems, in: 2013 IEEE International Symposium on Industrial Electronics, IEEE, 2013, pp. 1–6.

[32] M. Castilla, L. d.-V. Garcia, J. Miret, Microgrids design and implementation: Chapter 5; Control of power converters in AC microgrids; Chapter 5: Control of power converters in AC microgrids, Springer International Publishing (1st ed.), 2019.

[33] S. Golestan, J. M. Guerrero, J. C. Vasquez, A. M. Abusorrah, Y. Al-Turki, Modeling, tuning, and performance comparison of second-order-generalized-integrator-based flls, IEEE Transactions on Power Electronics 33 (12) (2018) 10229–10239.

[34] P. Rodriguez, A. Luna, I. Candela, R. Teodorescu, F. Blaabjerg, Grid synchronization of power converters using multiple second order generalized integrators, in: 2008 34th Annual Conference of IEEE Industrial Electronics, IEEE, 2008, pp. 755–760.

[35] W. S. Levine, The control handbook; Chapter 10: Design methods, CRC Press (vol. 1), 1996.

[36] D. G. Zill, Advanced engineering mathematics; Section 7.4: Cross product, Loyola Marymount University, Jones & Bartlett Learning (6th ed.), 2016.